



Parametric Optimization of a Cyclogiro Aircraft Design for Efficient Hover with Aeroelastic Considerations

Louis Gagnon¹, Marco Morandini², Stéphane Fournier³

¹Institute of Aerodynamics and Gas Dynamics, Universität Stuttgart, 70569, Germany, Email: gagnon@iag.uni-stuttgart.de

²Department of Aerospace Science and Technology, Politecnico di Milano, 20156, Italy, Email: marco.morandini@polimi.it

³Department of Aerospace Engineering, University of Bristol, BS8 1TR, United Kingdom, Email: stephane.fournier@bristol.ac.uk

Received November 27 2020; Revised March 22 2021; Accepted for publication March 22 2021.

Corresponding author: Louis Gagnon (gagnon@iag.uni-stuttgart.de)

© 2021 Published by Shahid Chamran University of Ahvaz

Abstract. A minimization procedure is proposed to orient the design of a vertical take-off and landing drone towards sustainability. The vehicle is a novel cycloidal rotor drone and the principal objective is to yield the best ratio of payload to power consumption. The drone blades, rotor arms, and frame are designed for fused deposition modeling additive manufacturing with polylactic acid. 10 variables for the geometry, operation parameters, and material infill percentages are explored in search of the optimum design. A special derivation procedure allows obtaining the symbolic equations for the weight and power consumption of the drone. This permits optimization with a hybrid genetic and gradient method and exploring a broad range of aircraft sizes. 7 constraint equations ensure that the necessary assumptions made for the derivation remain valid and that the structural strength is adequate. For each new configuration, this method allows to quickly find a new optimum design using a desktop computer. Also, modifying the constraints, variables, or objective function is straightforward. Finally, the resulting design has a power loading of 0.0876 N/W.

Keywords: Drones, Cycloidal rotors, Payload, 3D printing, Power loading.

1. Introduction

Unmanned aerial vehicles are currently getting a considerable amount of attention because of their recent mass commercialization. While traditionally being relied on for military purposes, they are now used in a variety of fields. Currently, widespread civilian applications are aerial photography, agriculture, and toys. There is a strong incentive to reduce their energy consumption because of their limited flight time. Nevertheless, little has been done to address the issue of power consumption and sustainability in general. A few attempts to obtain energy efficient configurations were done by propelling drones with cycloidal rotors instead of their traditional counterparts.

Cycloidal rotors are a viable means to produce aerodynamic forces whose direction can be rapidly varied 360° in a plane normal to the axis of rotation. They have been used in diverse aircraft [1, 2, 3] and micro aircraft [4, 5, 6, 7] prototypes. The working principle is illustrated in Fig. 1 and consists of a set of blades attached to a central drum. The superposition of two blade motions generates

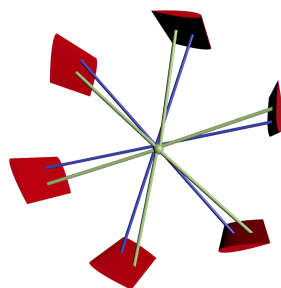


Fig. 1. Simplified cycloidal rotor.

the thrust. For one motion, the blades rotate about the rotor center while maintaining their span axes always parallel to the axis of the central drum. For the other motion, the blades individually pitch about their own pivoting axis with the same frequency as the main rotation. Changing the phase delay or the magnitude of their pitching motion allows almost instant thrust direction adjustments. The most frequent means to impose the pitching motion to the blades is with rigid links, as shown in Fig. 1. The central offset of these links generates the cyclic pitching motion of the blades.



While different cyclogiro aircraft were built [8, 9, 10, 11, 12, 1, 13], energy efficiencies providing a viable alternative to traditional helicopter rotary wings have generally been obtained only for micro aerial vehicles at low Reynolds number. Larger prototypes tend to have high disk loadings, and it negatively impacts energy efficiency. It is known [14] that the cycloidal rotor efficiency is highly dependent on rotor diameter, angular velocity, and other geometric parameters. However, an important parameter to consider in the case of flying vehicles is their weight, which directly influences the effective energy efficiency. Weight is interrelated with rotor dimensions and angular velocity, which changes the required structural strength. It was thus chosen to create a mathematical method to estimate the mass of drone and use it to iterate toward optimally efficient dimensions. The drone under study is to be almost entirely printed from polylactic acid (PLA) using the fused deposition modeling (FDM) method. PLA is chosen for its high rigidity, ease to print, and biodegradability. Special care is taken to maintain the whole mathematical procedure symbolic. Numerical integration is used only to find the center of gravity of NACA blades, but yields an analytic equation which remains equal when changing design parameters. Relying solely on symbolic equations is done in order to obtain the fastest solution possible. Although cycloidal rotors can be configured to respond rapidly, it was known from the start that the optimal configuration would not possess such a tactical advantage. This is due to the emphasis of this study on energy efficiency. Thus, a silent, stable, and controllable lifter for situations where energy consumption is a concern is sought.

The innovative contributions of this article are thus to: 1) present a highly maneuverable drone configuration by using cycloidal rotors; 2) use the environmentally friendly polylactic acid (PLA) for the blades, frame, and attachments of the drone; 3) optimize the whole design by using symbolic equations of effective payload lifted per unit of power while also considering the structural consequences of changing the dimensions, thicknesses, and angular velocities of the different parts of the drone.

2. Proposed design

The targeted drone design is shown on Fig. 2. This particular design was selected over different ones to obtain a stable drone

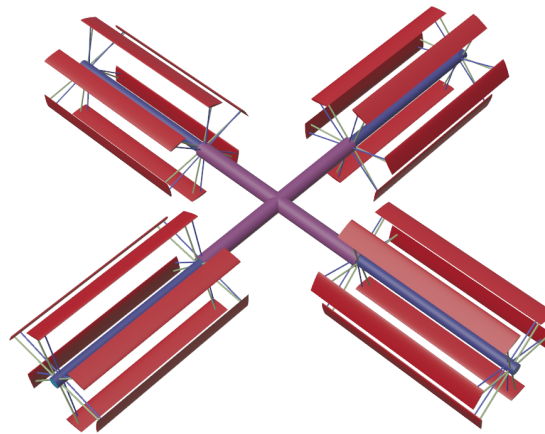


Fig. 2. Drone simplified design.

which can start a pitching or rolling motion instantaneously and without first yawing. A considerable control advantage this configuration is that the gyroscopic effects cancel out. The goal of this study is to optimize the geometry of the design in order to obtain the most efficient payload lift in hover. This is measured while having an onboard battery with a 5 minutes hover capacity at max payload.

In order to obtain a criterion to evaluate the energy efficiency of any UAV without bias introduced by its weight and size, a new indicator is proposed. That indicator is the ratio of the effective lift provided by the aircraft in hover to the total power it requires. That effective lift consists of the vertical thrust produced to which the weight has been subtracted. That indicator, here named the effective efficiency, is thus defined as,

$$\eta = F_{Tu} / \left(4 \frac{P}{n_m} N \right) \quad (1)$$

which has units of force per power and where N is the number of blades per rotor, P is the power required by each blade, n_m is the electric motor efficiency, and the effective lift force F_{Tu} is,

$$F_{Tu} = 4F_T N - m_t g \quad (2)$$

where g is the standard gravity, F_T is the thrust per blade, and m_t total mass of the aerial vehicle,

$$m_t = 4(Nb(m_b + m_s) + 2N(m_{rod} + m_{rod_p})) + m_m + m_{batt} + m_{ctrl} + 2m_{fr} \quad (3)$$

where m_b and m_s are the printed blade and aluminum spar masses per unit span, respectively, m_{batt} is the mass of the battery, m_{ctrl} is the mass of the controller, m_{rod} is the mass of each control rod, m_{rod_p} is the mass of each pivot rod, m_{fr} is the mass of each of the two frame beams constituting the main "+" drone axis, m_m is the overall motor mass, and b is the blade span. It is assumed that the pitch and pivot rods have the same design and thus the same masses.

The principal components of the drone are included in the optimization procedure to have an accurate weight estimate. As shown in Fig. 2, the aircraft has 4 rotors placed in a "+" configuration, the frame beams have a circular cross-section, and a set of 4 cylindrical rods hold and pivot each blade. For the scope of this study, no fuselage is considered and the structure is limited to the frame beams. These two cylindrical frame beams have partially filled inner portions, as shown in Fig. 3. With R being the radius of a rotor and c the blade chord, the first attachment point of each rotor is $R + c$ away from the center. The beam radius reduces after crossing the inner rotor attachment point. The blades are also partially filled and are reinforced with inner aluminum spars as shown in Fig. 4.



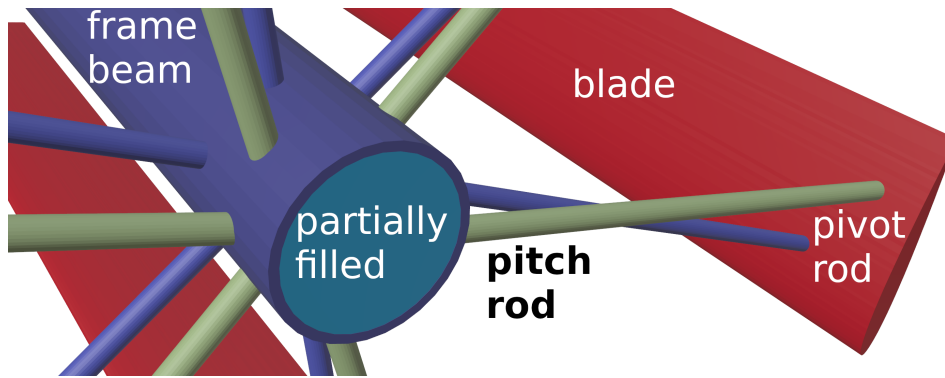


Fig. 3. Close-up on the frame.

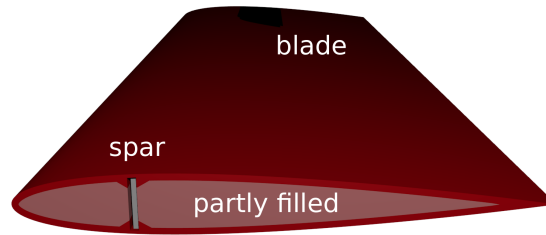


Fig. 4. Blade design with spar.

3. Mathematical development

This section shows the mathematical developments necessary to obtain a fully symbolic equation that can be fed to the optimization algorithms. The passages of the derivations which are taken from other studies [15, 16] are omitted from this paper. The reader is encouraged to consult the original studies to obtain a deeper understanding of the mathematical derivations of the cycloidal rotor aerodynamic equations. Although different units are occasionally given in the tables, the computations of this study are done using radians and SI base units.

3.1 Exploration domain and fixed parameters

The parameters of the drone which were allowed to change during the optimization are first given as an introduction to the model. Table 1 lists the 10 optimization variables, their allowed ranges, and their definitions. Most of these ranges were chosen to

c	blade chord	0.02	0.2	m
θ_c	pitch function magnitude	0.57	90	°
R	rotor radius	0.05	0.5	m
N	number of blades per rotor	2	6	-
Ω	angular velocity of the rotors	2	500	rad/s
A_{rod}	area of the pitch and pivot rods	5×10^{-7}	10^{-4}	m ²
b	blade span	0.03	0.25	m
p_i	blade infill percentage	10	90	%
p_{i_f}	frame infill percentage	10	90	%
r_s	spar thickness to height ratio	0.04	5	-

Table 1. Optimization variables.

ensure that the design assumptions are still valid for the given dimensions, that geometric constraints are respected, and that the resulting aircraft is micro or small in size. The number of blades was limited to 6 because no design with more blades is seen in the literature. A similar reasoning was done for the maximum allowed angular velocity. The infill percentage was limited to 90% because of the available data and the negative structural impacts of working at 100% infill. Nevertheless, the exploration domain can be extended for designers who wish to do so. For example, as the results presented later will suggest, a concept with more blades could be considered. As for the variables that have a fixed value and are not optimized, they are defined in Table 2. Some of them, such as air density and controller weight, are fixed by nature. Other variables, such as material properties and geometric parameters, are fixed to maintain the continuity of the equations.

A conservative estimate of motor efficiency is used in order to ensure that possible imprecisions lead to an underestimation of efficiency. For the same reason, the coefficient of lift used for the blade deformation calculations is taken at the maximum angle of attack, $C_L = \alpha_m a$, as opposed to the accurate lift coefficient used for the thrust calculation. The threshold t_{bt} is the maximum allowed pitch angle difference between the blade root and tip due to its dynamic torsion. This threshold ensures that the aerodynamic coefficients variations along the blade are negligible. The aspect ratio of the rods, r_{rod} , is fixed in order to avoid requiring numerical root finding. The minimum allowed total thickness of the filled outer printed layers, t_f , is set to the thickness of 3 printed PLA layers. This chosen number arises from experiments conducted with the Bluetek Strato 3D printer and applies to the blades, the rods, and the frame beams.



κ	1.48	empirical multiplier for flow non-uniformity and tip losses
ρ	1.204	air density (kg/m ³)
a	5.5	slope of the lift coefficient against the angle of attack (1/rad)
E_s	70×10^9	alu. spar Young's modulus (Pa)
ρ_s	2650	aluminum spar density (kg/m ³)
ρ_{pla}	1250	PLA density (kg/m ³)
t_{bt}	0.01	threshold of admissible pitch angle multiplier at blade tip
$p_{i_{rod}}$	100	percent infill of printed PLA pitch and pivot rods
r_{rod}	0.25	pivot rod thickness to height ratio
ν_b	0.37	Poisson's ratio estimate for PLA
n_m	0.8	motor efficiency
m_{ctrl}	0.050	controller weight (kg)
t_f	1.20	thickness of filled PLA layers (mm)
η_{sb}	1.5	safety factor for frame beams
η_{sr}	1.2	safety factor for the pitch and pivot rods

Table 2. Fixed parameters of the optimization.

3.2 Aerodynamics

The calculation starts from the implicit thrust equation¹ of Gagnon *et al.* [15], corrected for proper drag coefficient consideration by changing the $\frac{C_D}{a}$ term to $\frac{C_D}{\sigma a}$. Being in hover, a null advance ratio $\mu = 0$ is used. That thrust equation thus has the form

$$\left(\frac{\frac{4C_T}{\sigma a} - \theta_c}{\left(\frac{C_D}{\sigma a} + 1 \right) \kappa} \right)^2 - \pi \frac{C_T}{2} = 0 \quad (4)$$

where C_T is the thrust coefficient, rotor solidity is $\sigma = cN/(2\pi R)$ and κ is an empirical term that accounts for non-uniformity and tip losses. Use of similar correlation terms is common, as seen in [17] and [18]. The κ term is fixed to the conservative value of $\kappa = 1.48$ during the entire iterative process of this project. As such, tip losses are assumed to be amongst the highest seen experimentally. This is demonstrated by the correlation between numerical and experimental cycloidal rotor data [15] where values of κ varied between 1.08 and 1.48. Once again, this is done to estimate to worst possible energy efficiency. Thus, Eq. (4) is solved for thrust C_T and the only real root is kept. The reader is invited to solve for the real root of C_T on their own because the result is too bulky to give in this article.

The inflow coefficient for a hover case is

$$\lambda = \sqrt{\pi \frac{C_T}{2}} \quad (5)$$

which allows solving for the max angle of attack,

$$\alpha_m = \theta_c - \tan^{-1}(\lambda) \quad (6)$$

where θ_c is the magnitude of the pitch function. The maximum aerodynamic forces equation, taken from Gagnon *et al.* [16] is,

$$f_a = \frac{\rho}{2} (\Omega R)^2 c C_L \quad (7)$$

where C_L is the lift coefficient and is estimated as $\alpha_m a$ to get the maximum value. The drag aerodynamic forces on a blade, neglecting the effects of flow curvature [19], are

$$f_d = \frac{\rho}{2} (\Omega R)^2 c C_D \quad (8)$$

where C_D is a drag coefficient that depends on the Reynolds number and is defined later in Eq.(77). The force tangential to each blade's path, $F_{r_{x0}}$, and the thrust per blade, F_T , knowing the coefficient of thrust C_T , are also taken from the aerodynamic analysis of Gagnon *et al.* [15]. Knowing these variables, the power required to rotate one blade is

$$P = F_{r_{x0}} R \Omega \quad (9)$$

Now that the power and thrust are known, the structural aspects are addressed.

3.3 Structure

Weight is estimated from the contributions of the different parts that constitute the drone. It is known that the structural properties of the FDM PLA differ from those of injection molding and that the direction of printing influences them, but the specific data is currently not available in the scientific literature. Thus, the yield stress of the printed PLA frame is estimated, in N/m², using a curve derived from a technical report made available online by Arts et Métiers ParisTech [20] as

$$\sigma_{by} = 10^6 \left(8 + 20(p_{i_{fr}} - 10)/80 \right) \quad (10)$$

where $p_{i_{fr}}$ is the infill percentage of the inner layers of the frame beams. An equivalent equation gives the blade yield stress. And, it is assumed that, unlike for the ultimate strength, the yield strength of a blade does not diminish if printed in the spanwise direction.

¹The referred article presents it as Eq. (64).



3.4 Rotor blades

The blades of the rotor are the most critical part of the design. They have to sustain high centrifugal loads and resist torsion induced by the pitching motion. This section presents the core of the analysis conducted on the blades.

The blade height is $0.01N_n c$ where N_n is the NACA number. The minimum blade height to have a non-filled inner portion is that of 3 printed layers on top and 3 more at the bottom. Knowing that each printed PLA layer is 0.4 mm, the totally filled height is consequently $h_f = 2t_f = 2.4$ mm, where t_f is the thickness of 3 filled layers. Thus, to maintain the continuity of the equations to solve, the minimum chord for which the equations shown here are valid is

$$c_{min} = 2t_f / \left(\frac{N_n}{100} \right) \tag{11}$$

and the height of the partially filled inner portion of the blade, and consequently of the blade spar, is

$$h_s = h_b - h_f \tag{12}$$

where h_b is the outer height of the blade. Also, the chordwise thickness of the spar is $t_s = h_s r_s$ where r_s is the aspect ratio of the spar. The chord of the inner blade area is not only reduced by the thickness of the filled layers, but also by the junction of the upper and lower skins at its trailing edge. Therefore, is estimated twice, once by overestimating,

$$c_{i_o} = c - h_f \tag{13}$$

and once by underestimating,

$$c_{i_u} = (h_b - h_f) / \left(\frac{N_n}{100} \right) \tag{14}$$

Now, choosing to rely on the exact blade moments of area, the thicknesses of the inner and outer portions of the blades are obtained. The outer blade half thickness along the chord is,

$$f_x = \frac{\sqrt{cx}N_n}{67.363} - \frac{xN_n}{158.73} - \frac{x^2N_n}{56.883c} + \frac{x^3N_n}{70.348c^2} - \frac{x^4N_n}{193.05c^3} \tag{15}$$

which comes from the standard NACA symmetric airfoil equation and where x is the distance from the leading edge along the chord. The inner, partially filled, half thickness of the blade along the chord, $f_{x_{pi}}$, is obtained by substituting $c = c_{i_u}$ in Eq. (15). Thus, the cross-section area of the full blade is,

$$A_b = \int_0^c 2f_x dx \tag{16}$$

While, similarly, the cross-section area of the partially filled PLA blade is,

$$A_{b_{pi}} = \int_0^{c_{i_u}} 2f_{x_{pi}} dx \tag{17}$$

An area parameter for the full blade is defined as,

$$K_a = A_b / \left(\frac{N_n}{100} c^2 \right) \tag{18}$$

The second moment of area of a blade section about the chord is thus,

$$I_{b_A} = \int_0^c \int_{-f_x}^{f_x} y^2 dy dx \tag{19}$$

where y is the vertical distance from the blade's reference axis. And the moment of inertia per unit span about the nose of a completely filled blade is,

$$I_{b_{Bnosef}} = \rho_{pla} \int_0^c \int_{-f_x}^{f_x} (x^2 + y^2) dy dx \tag{20}$$

while for a partially filled blade it is,

$$I_{b_{Bnosepi}} = \frac{p_i}{100} \rho_{pla} \int_0^{c_{i_u}} \int_{-f_{x_{pi}}}^{f_{x_{pi}}} (x^2 + y^2) dy dx \tag{21}$$

Which leads to the moment of inertia about the pivot point,

$$I_{b_p} = I_{b_{Bnosef}} + \rho_{pla} A_b \left((x_p - x_{cg})^2 - (x_{cg} - x_n)^2 \right) \tag{22}$$

where x_p , x_{cg} , and x_n are the distances of the pivot point, center of gravity, and nose from the leading edge of the blade, respectively. Thus, $x_n = 0$. For symmetric 4 number NACA blades, $x_{cg} = d_{naca} c$, where $d_{naca} = 0.4015$, according to an online derivation². Also, the moment of inertia about its centroid is,

$$I_{b_{Bcgf}} = I_{b_{Bnosef}} - \rho_{pla} A_b (x_n - x_{cg})^2 \tag{23}$$

Similarly, for the inner partially filled portion of the blade, the moment of inertia per unit span about the center of gravity of the outer blade is,

$$I_{b_{Bcgpi}} = I_{b_{Bnosepi}} - \frac{p_i}{100} \rho_{pla} A_{b_{pi}} \left((d_{naca} c_{i_u})^2 - (d_{naca} (c - c_{i_u}) - \frac{h_f}{2})^2 \right) \tag{24}$$

²<http://louisgagnon.com/scBlog/airfoilCenter.html>



And finally, for the complete blade which has filled outer layers and partially filled inner layers, one obtains,

$$I_{bBcg} = I_{bBcgf} - I_{bBcgp_i} \left(\frac{100}{p_i} - 1 \right) \quad (25)$$

The blade torsion factor, as defined by Young et al. [21], is

$$K_b = 4I_{bA} / (1 + 16I_{bA} / (K_a h_b c^3)) \quad (26)$$

The Young's modulus, derived from [20], for the blades, E_b , the pivot rods, E_{rod} , and the frame beams, E_{fr} , are defined as

$$E_z = 10^9 (0.6 + 2.5(p_{iz} - 10)/90) \quad (27)$$

substituting p_{iz} by the adequate variable of infill percentage. Then, the modulus of rigidity of a PLA blade, G_b , is obtained by assuming that the material is isotropic. And, assuming that the beam is perfectly bound at the filled to non-filled intersection, the flexural rigidity is,

$$EJ_e = E_b I_{bA} + E_s J_s \quad (28)$$

where $J_s = \frac{1}{12} t_s h_s^3$ is the spar section second moment of area about its centroid line. The spar mass per unit span is,

$$m_s = t_s h_s \rho_s \quad (29)$$

and the total, blade plus spar, mass per unit span is,

$$m = m_b + m_s \quad (30)$$

We assume that the blades are simply supported, thus taking an equation³ from Gagnon et al. [16] the blade centrifugal displacement at midspan is obtained as

$$q_w = R\Omega^2 \left(\frac{4}{\pi} \left(1 + \frac{1}{2}A \right) \right) / (\pi^4 EJ_e / (mb^4) - \Omega^2(1 + A)) \quad (31)$$

where $A = \rho c_L R/m$. The blade deformation along the span is

$$w = \cos\left(\frac{\pi}{b}x\right) q_w \quad (32)$$

The maximum magnitudes of the strain in the blade, ϵ_b , and in the spar, ϵ_s , are,

$$\epsilon_z = \left| \frac{h_z}{2} \frac{d^2 w}{dx^2} \right| \quad (33)$$

substituting h_z by the proper height variables. The maximum absolute axial stress in the blade, σ_b , and in the spar, σ_s , looking at both compression and tension, is thus,

$$\sigma_z = E_z \epsilon_z \quad (34)$$

substituting E_z and ϵ_z by the appropriate variables. Finally, the bending moment in the blade is,

$$M = EJ_e \frac{d^2 w}{dx^2} \quad (35)$$

3.5 Blade torsion delay

In the current design, blade pitch is imposed only on one end of the blade. Thus, the rigidity in torsion must be sufficient to maintain reasonable pitch angle differences between the blade tip that is controlled and the other one. Differences from the requested angle are known to cause efficiency losses. The derivation follows the setup shown in Fig. 5. One defines

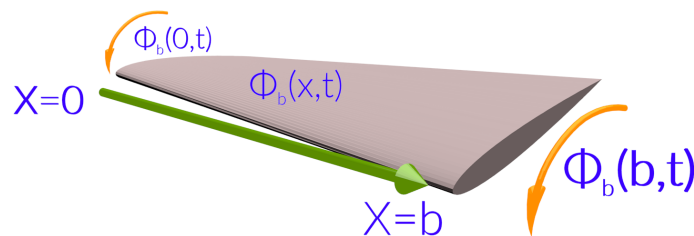


Fig. 5. Problem setup for dynamic torsion of blade.

$$\phi_b(x, t) = \phi_b(0, t) + \Delta\phi_b(x, t) \quad (36)$$

where $\phi_b(x, t)$ is the pitch angle along the blade and $\Delta\phi_b(x, t)$ is the pitch angle difference with respect to the controlled end. The imposed pitch angle at the controlled end is, for the current case,

$$\phi_b(0, t) = \theta_c \cos(\Omega t + \phi) = \theta \quad (37)$$

³The referred article presents it as Eq. (8).



where ϕ is the phase angle of the pitch function. By differentiating Eq. (36) twice with respect to time and twice with respect to distance, one obtains

$$\ddot{\phi}_b(x, t) = \ddot{\theta} + \Delta\ddot{\phi}_b(x, t) \tag{38}$$

$$\phi_b''(x, t) = 0 + \Delta\phi_b''(x, t) \tag{39}$$

respectively. From the principle of virtual work, it is known that

$$K_b G_b \theta'' = I_{b_{Bcg}} \ddot{\theta} \tag{40}$$

recalling that K_b is the torsion factor defined in Eq. (26) and G_b is the modulus of rigidity. Substituting in the proper values, one obtains,

$$K_b G_b \Delta\phi_b''(x, t) - I_{b_{Bcg}} \Delta\ddot{\phi}_b(x, t) = -I_{b_{Bcg}} \theta_c \Omega^2 \cos(\Omega t + \phi) \tag{41}$$

The variable of interest is $\Delta\phi_b$ and a boundary value problem is thus set up. The form of the equation is posed as,

$$\Delta\phi_b = f(x) \theta_c \cos(\Omega t + \phi) \tag{42}$$

with

$$f(0) = 0 \quad f'(L) = 0 \tag{43}$$

and thus,

$$\Delta\phi_b'' = f''(x) \theta_c \cos(\Omega t + \phi) \tag{44}$$

$$\ddot{\phi}_b = -f(x) \Omega^2 \theta_c \cos(\Omega t + \phi) \tag{45}$$

which is substituted into Eq.(41) to yield

$$K_b G_b f''(x) + I_{b_{Bcg}} f(x) \Omega^2 = -I_{b_{Bcg}} \Omega^2 \tag{46}$$

and rearranging gives

$$\frac{K_b G_b}{I_{b_{Bcg}} \Omega^2} f''(x) + f(x) = -1 \tag{47}$$

for which the particular solution is

$$f_p = 1 \tag{48}$$

and the homogeneous solution is

$$f_h = A \cos(\zeta x) + B \sin(\zeta x) \tag{49}$$

where

$$\zeta = \Omega \sqrt{\frac{I_{b_{Bcg}}}{K_b G_b}} \tag{50}$$

and finally, solving for A and B using the boundary conditions of Eq.(43) and substituting back into Eq.(42) yields

$$\Delta\phi_b = (\cos(\zeta x) + \tan(\zeta b) \sin(\zeta x) - 1) \theta_c \cos(\Omega t + \phi) \tag{51}$$

which expresses the difference of angle between the blade attachment point and its free edge for the excited cycloidal rotor. To obtain the blade natural frequency in torsion, Eq.(51) is inspected knowing that the $\theta_c \cos(\Omega t + \phi)$, the $\cos(\zeta x)$, and the $\sin(\zeta x)$ terms cannot diverge. This leaves the $\tan(\zeta b)$ to inspect and yields that the first natural frequency in torsion occurs at

$$n_{bt} = \pi / (2b) \sqrt{K_b \frac{G_b}{I_{b_{Bcg}}}} \tag{52}$$

The part of Eq. (51) which is constant in time but variable along the span, x , is further inspected. Setting the derivative with respect to x of this part of the equation to zero and dividing by $\cos(\zeta x)$ yields

$$\tan(\zeta x) = \tan(\zeta b) \tag{53}$$

Inspection of Eq. (53) by referring to Eqs. (52) and (50) indicates that, for any frequency equal or below the natural frequency, the pitch angle delay does not reach a maximum before the tip of the blade at $(x = b)$. Thus, until the natural frequency is surpassed, the torsional deformation will always increase along the span, without changing direction. Also, in the absence of a pitch function phase delay, this will occur at $t = \{0, 2\pi, 4\pi, \dots\}$ s and the pitch angle difference remains a multiplicative factor of the imposed pitch angle in time. This multiplicative factor grows with the frequency. Thus, the ratio of rotation frequency to natural frequency where threshold gets exceeded at blade tip is given by,

$$r_{t_{bt}} = \sec^{-1}(1 + t_{bt}) \frac{2}{\pi} \tag{54}$$

where t_{bt} is the threshold of admissible pitch angle multiplier at blade tip. Finally, the maximum stress in the blade due to torsion, by performing an uncoupled analysis, using the equations of Young et al. [21] is,

$$\tau_{b_m} = G_b \frac{\phi_{b_{max}}}{b} C_y \tag{55}$$

where C_y is a constant defined by Young et al. and is based on the blade curvature at the point where the largest inscribed circle touches the blade profile.



3.6 Pitch and pivot rods

The centrifugal forces per unit span on a blade are,

$$f_c = m\Omega^2 R \quad (56)$$

The maximum force acting axially on one pivot rod, which holds the blades and imposes the rotation, assuming that $f_a < f_c$, and also assuming that the forces from the pitch rods have no influence on the blade bending, is

$$f_{rod_{max}} = (f_c + f_a) \frac{b}{2} \quad (57)$$

The minimum required torque for the electric motor, assuming that it is operating at the angular velocity able to provide its rated torque, is

$$T_{motor} = 4PN/\Omega \quad (58)$$

Knowing that two pivot rods transmit the motor torque to each blade and assuming that the torque will never exceed the necessary value for the blade to rotate, the torque transmitted by each pivot rod is,

$$T_{rod} = P/2\Omega \quad (59)$$

Finally, a feasible design can only be achieved if the constraint,

$$\sigma_{rod_{c1}} = \frac{\eta_s}{A_{rod}} \left(f_{rod_{max}} + T_{rod} 6 \sqrt{\frac{r_{rod}}{A_{rod}}} \right) - \sigma_{rod_y} \leq 0 \quad (60)$$

where σ_{rod_y} is the yield stress of the material. The strain ratio of the pivot rods is defined as,

$$\epsilon_{rod} = \frac{f_{rod_{max}}}{A_{rod}} / E_{rod} \quad (61)$$

and the pivot rod wide edge as,

$$d_{rod} = \sqrt{\frac{A_{rod}}{r_{rod}}} \quad (62)$$

and its narrow edge as,

$$b_{rod} = r_{rod} d_{rod} \quad (63)$$

The moment of inertia of the pivot rod is $I_{rod} = b_{rod} d_{rod}^3 / 2$ where the inner portion is considered as if it were filled, to be conservative. This causes both the deformation and the stress inside the rod to be slightly overestimated. Thus, the max rearward deflection of the rod is at the pivot point, which is the point of attachment with the blade, and is,

$$w_{rod} = T_{rod} b_{rod}^2 / (3E_{rod} I_{rod}) \quad (64)$$

while the combined maximum stress inside the rod is,

$$\sigma_{rod} = \frac{f_{rod_{max}}}{A_{rod}} + T_{rod} \frac{d_{rod}}{2I_{rod}} \quad (65)$$

Finally, the mass of the pivot rod is simply $m_{rod} = A_{rod} R \rho_{pla}$.

3.7 Frame beams

The principal structure of the frame consists of the printed tubular beams shown in blue in Figs 2 and 3. The first section of the beam reaches the inner attachment point of the rotor and has a radius R_{fr1} . The remainder of the beam has a radius of R_{fr2} . Each rotor beam is subjected to symmetric loads and is thus analyzed as an equivalent cantilever beam having half the length and being rigidly supported at the middle of the "+" frame. Along with the conditions imposed in Section 2., the frame's inner and outer beam section half lengths are thus $L_{fr1} = R + c$ and $L_{fr2} = b$, respectively. Their sectional second moments of area are computed as if they were partially filled and had no external 100% filled layers,

$$I_{fr} = \frac{\pi}{4} \left(R_{fr}^4 \right) \frac{P_{ifr}}{100} \quad (66)$$

where R_{fr} is the radius of the beam section. Assuming the external layers of the printed beams to be partially filled for the calculation of I_{fr} allows maintaining a fully analytic solution, but slightly overestimates the maximum stress. The overestimation comes from the fact that $I_{fr_{out}}$ is underestimated by the model and thus the Euler-Bernouli beam theory overestimates the radius of curvature as,

$$R_k = M_{fr} / (E_{fr_{in}} I_{fr_{in}} + E_{fr_{out}} I_{fr_{out}}) \quad (67)$$

where the *in* and *out* subscripts indicate the inner and outer portions of the beam, respectively. In turn, the theory gives that the stress in the frame beam can be expressed as,

$$\sigma_{fr} = y_{n_{fr}} E_{fr} \frac{d^2 w_{fr}}{dx_{fr}^2} = y_{n_{fr}} E_{fr} R_k \quad (68)$$

where $y_{n_{fr}}$ is the distance from the beam's neutral axis. Equation (68) indicates that for the beam made of a partially filled inner cylinder held into a filled outer hollow cylinder, both having a constant Young's modulus, the maximum stress will be either at their interface or at the outer edge. In the current case, Young's modulus is modeled as constant and is in any case greater for the outer section. Thus, the maximum stress is at the outer section is overestimated by the model. It is thus conservative.



The maximum force sustained by each frame arm at its point of attachment with a rotor is sought. It is the sum of the 2 rod forces per blade multiplied by the number of blades and divided by 6 to account for the fact that the maximum forces are generated during a sixth of the cycle, as noted in the computational fluid dynamics study of Gagnon et al. [22]. That total force is thus,

$$F_{fr} = f_{rod_{max}} \frac{N}{3} \tag{69}$$

which is equivalent to having an additional safety factor of 2 on the frame forces. The frame half beams are assumed to be each taking the load generated by two rotor attachment points. The stress in the frame is set to be the yield stress, to have the lightest feasible structure, and thus solving

$$\eta_{sb} F_{fr} (2L_{fr1} + L_{fr2}) R_{fr1} / I_{fr1} - \sigma_{fry} = 0 \tag{70}$$

and

$$\eta_{sb} F_{fr} L_{fr2} R_{fr2} / I_{fr2} - \sigma_{fry} = 0 \tag{71}$$

gives the radius of the inner and outer beam sections, respectively. The multiplication by the safety factor η_{sb} ensures a stronger design. Conversely, the deflections at the tip of the inner and outer beam sections are equivalent to a cantilever beam with a tip load of F_{fr} and $2F_{fr}$, respectively. The tip deflection of the beam sections, considered static under the maximum force F_{fr} at the attachment point, are,

$$w_{fr_{beam,1}} = 2F_{fr} L_{fr1}^3 / (3E_{fr} I_{fr1}) \tag{72}$$

$$w_{fr_{beam,2}} = F_{fr} L_{fr2}^3 / (3E_{fr} I_{fr2}) \tag{73}$$

and their sum gives the displacement at the outer tip of the rotor. Two roots of each Eqs. (70) and (71) are always complex conjugates that have a null real part. The third roots are always real for positive variables. The optimal radii of the frame are thus found by algebraically solving and retaining the only non-imaginary solution to the cubic equation. The inner radius of the frame beam sections can thus be computed as,

$$R_{fri} = R_{fr} - t_f \tag{74}$$

Finally, the mass of one full frame beam is,

$$m_{fr} = 2\rho_{pla}\pi \left(L_{fr1} \left(R_{fr1}^2 + R_{fri}^2 \frac{p_{ifr} - 100}{100} \right) + L_{fr2} \left(R_{fr2}^2 + R_{fri}^2 \frac{p_{ifr} - 100}{100} \right) \right) \tag{75}$$

3.8 Constraints and other functions

To maintain the validity of the blade drag and lift estimates, the maximum admissible angle of attack is limited in function of the Reynolds number. This angle consists of the fitted curve on airfoil data collected from the XFLR5 toolkit⁴ which is based on Xfoil. The points of maximum allowed angle of attack were taken as those where the lift coefficient curve ceases to be linear. It has the following form,

$$\alpha_{ma} = a_{coef} + b_{coef} Re^{\frac{1}{2}} + c_{coef} Re + d_{coef} Re^2 \tag{76}$$

A similar curve fitting procedure using XFLR5 is done for the drag coefficient, which is assumed to be a function of only the Reynolds number. The drag coefficient values are thus taken at an angle of attack of 5°, and fitted to a curve of the following form,

$$C_{D_{fit}} = a_{coef2} Re^{-1} + b_{coef2} + c_{coef2} Re + d_{coef2} Re^{\frac{1}{2}} \tag{77}$$

Another data fitting procedure is done to obtain the mass of the motor as a function of its power. The data used for the curve fitting is gathered from diverse online retailers of drone motors. The data indicates that the relationship between weight and power is linear, thus,

$$m_m = (a_{coef3} + b_{coef3} P_{out}) / 1000 \tag{78}$$

where the required output power from the motor is,

$$P_{out} = 4P \frac{N}{n_m} \tag{79}$$

The battery mass is estimated as,

$$m_{batt} = P_{out} \frac{600}{3600} / 130 \tag{80}$$

assuming 130 Wh/kg for typical drone LiPo batteries and a required 5 min autonomy at full load. The Mach number is simply defined as,

$$Ma = \frac{\Omega R}{340.29} \tag{81}$$

The chord to circumference ratio is also computed to verify that the blades are not dangerously close to each other,

$$c_c = Nc / (2\pi R) \tag{82}$$

However, the blade aspect ratio is not constrained, because it is known [23] to have little influence on the aerodynamics of cycloidal rotors. This concludes the setup of the constraints for the optimization problem. Their values should not surpass zero. Most of the equations presented were solved with the SageMath [24] computerized symbolic math toolbox. The results are especially bulky, partly because of from multiple integrations of the function of the NACA profile. The reader is thus spared the presentation of the final equations, which can be obtained by reproducing the steps presented so far.

⁴www.xflr5.com



4. Solution Process

4.1 Problem setup

A particular design strategy is relied upon for this preliminary sizing study and differs from a more traditional approach. The goal is to maximize the payload efficiency instead of limiting the analysis to only carry the weight of the aircraft. This is done to identify the highest achievable energy efficiency to transport cargo, regardless of the total mass to be carried per individual drone.

Thus, with all the necessary equations established, the problem is formulated as the minimization of one objective function subject to seven constraint equations. The objective function to minimize is the negative effective payload efficiency, $\eta_c = -\eta$, in N/W , where η was defined in Eq. (1). The constraints are imposed as one-sided nonlinear constraints. Penalties are attributed to ensure the constraint equations do not surpass zero. The constraints are summarized in Table 3. As for the optimization variables, their ranges were previously given in Table 1.

$\alpha_{m_c} = \alpha_{m_f} - \frac{\alpha_{m_a}}{180} \pi$	max. angle of attack
$Re_c = 40\,000 - Re$	min. Reynolds number
$\sigma_{rod_c} = \sigma_{rod_{c1}}$	max. internal stress on the rods
$\sigma_{b_c} = \sigma_b^2 - \sigma_{b_y}^2$	max. internal stress on blades
$\sigma_{s_c} = \sigma_s^2 - \sigma_{s_y}^2$	max. internal stress on spars
$\tau_{b_{m_c}} = \tau_{b_m} - \sigma_{b_y}$	max. blade stress from torsion
$\Omega_{t_{m_c}} = \Omega - r_{t_{bt}} n_{bt}$	max. frequency to maintain a reasonable blade torsion angle

Table 3. Optimization constraints.

Once the setup is ready, the symbolic equations are generated in C++ format with SageMath. The code is then compiled and the optimization is run.

4.2 Optimization

The objective function, the 7 constraint equations, and the 10 parameter ranges are fed to a minimization procedure. All the optimizations discussed in this paper are performed using Sandia's Dakota [25] toolbox. Different approaches were tested to retain the one which consistently yields the global optimum, regardless of the starting point and the allowed ranges.

The analytical gradients are easily obtained because the equations are symbolic. Thus, different gradient methods (GM) were tested. However, the presence of many local minima was observed and thus GM seldom provide the best solution. Consequently, a 3-step hybrid method consisting of a genetic algorithm (GA), followed by a pattern search, and followed by a GM, was attempted. Yet, the pattern search algorithm did not improve the intermediate solution. Also, the capability of the GM to obtain the global solution depends on the output of the preceding GA.

Thus, an approach where multiple solutions are fed to the GM was attempted. However, better minima are obtained when running one instance of the GA with a high number of iterations and feeding the results to the GM and not when feeding the GM with several outputs of the GA obtained with fewer iterations.

Different attempts at changing the algorithm parameters were tested: larger populations; allowing up to 10 million function evaluations; and, a CHC⁵ population replacement type instead of the elitist one. Ultimately, it turned out that the Single-objective Genetic Algorithm (SOGA) was able to provide consistently good solutions.

The retained optimization method consists of manually multi-starting a combination of SOGA followed by a the feasible directions gradient method [26]. The first starts of the SOGA rely on population of 1024 individuals with a high mutation rate and a selection procedure which favors feasible designs. As the multi-start solutions accumulate, the population size is gradually increased and the exploration domain is restrained to include only the range of values returned as optimal by the preceding runs. As such, the variables for percent infill of the PLA, the number of blades, and the spar aspect ratio are fixed during the last multistart iterations because the optimum consistently return their limit values. The thus conducted final GA-GM iterations all lead to optima which have their objective, the effective efficiencies η , less than 1% away from the final optimum. This happens thanks to the large population of 15,625 and the restrained exploration domain. This percentage indicates a very small rotor efficiency difference, because most tested conditions actually return $\eta < 0$ as the thrust generated by the rotors does not overcome the aircraft weight.

5. Results and discussion

The resulting geometry is shown to scale in Fig. 6 and Tables 4 to 7 give the optimized input variables, masses, geometry, and structure, respectively.

c	2.01 cm
θ_c	14.9 °
R	22.2 cm
N	2
Ω	282 rad/s
A_{rod}	1.99 mm ²
b	3.80 cm
p_i	90.0%
p_{i_f}	90.0%
r_s	0.0400

Table 4. Optimized variables.

⁵In the CHC approach, the retained population consists of the best parents and new individuals along with a random sample from the available solution set.



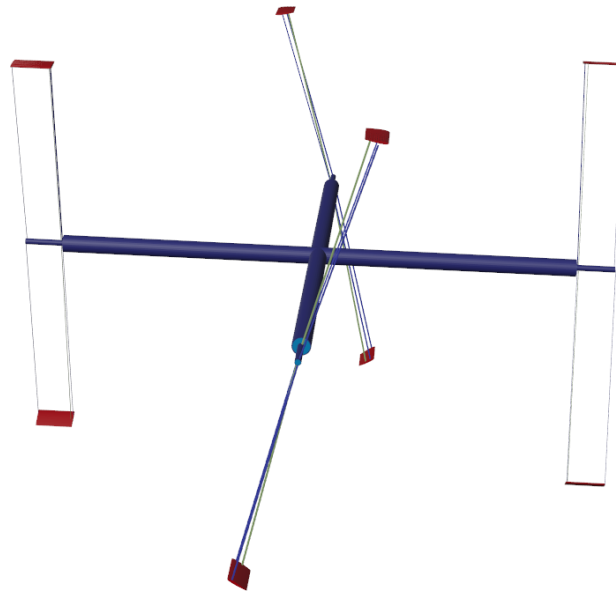


Fig. 6. Optimized drone structure, payload and components not shown.

m_t	total drone mass	349 g
$m_{b,b}$	PLA blade mass	1.38 g
m_m	motor mass	11.5 g
m_{batt}	battery mass	85.4 g
$2m_{fr}$	frame mass	173.7 g

Table 5. Optimized masses.

The resulting configuration of Fig. 6 has an effective hover efficiency $\eta = 0.01864$ Newtons of payload per Watt provided to the electric motor at the maximum payload of 127 g. This is equivalent to 1.90 kg/kW which is not to be confused with the power loading, for which the value is 8.93 kg/kW, because it does not subtract aircraft weight and electric motor losses. The rotor requires a total power, at maximum payload, of 53.3 W. At this flight condition, the Mach number is 0.184 and the Reynolds number is 86,059. The estimated maximum coefficient of lift C_L used only for the structural calculations is 0.957, assuming operation at the maximum angle of attack. The average aerodynamic thrust produced per blade is 0.584 N. The centrifugal blade force is roughly 13 times larger than the maximum expected aerodynamic force generated by a blade. This verifies the initial assumption which allowed neglecting buckling of the pitch and pivot rods in the calculations. The resulting dimensions of the pitch and pivot rods are, however, challenging for a typical FDM printer. A final design should consider using readily available plastic or composite rods instead. Finally, the rotor disk loading is 7.05 kg/m² and the figure of merit calculated using the momentum theory of a conventional rotor is 0.470. Both power and disk loading are calculated using $2Rb$ as the reference disk area. The obtained figure of merit is typical for cycloidal rotors [27] without individual pitch control and indicates that the optimization conducted here rather relies on reducing the disk loading to gain efficiency.

5.1 Efficiency comparison

Beyond the measure of efficiency η peculiar to this study, a more general measure of efficiency is calculated as the ratio of total aerodynamic thrust to power consumed by the motor, $\eta_{tot} = 0.0701$ N/W. This number is often referred to as power loading, and if the electric motor losses are ignored, it becomes $\eta_{max} = 0.0876$ N/W. The three measures of efficiency obtained, η , η_{tot} , and η_{max} , are compared to other vertical take-off and landing aircraft from the literature. In comparison, the world’s most efficient manned helicopter, the Atlas [28], has $\eta = 0.98$ N/W and $\eta_{tot} = 1.70$ N/W, approximately. That human-powered helicopter carries a 75 kg payload which in this particular case also serves as its motor and battery, has a 50 m aircraft span, and takes advantage of the ground effects to reduce the required power. Elsewhere, a computational fluid dynamics study [2] reported up to $\eta_{max} = 0.208$ N/W for very low rpm cycloidal rotors having radii of 0.5 m. A parametric experimental study [29] of cycloidal rotors with radii ranging from 5 cm to 12.7 cm reached $\eta_{max} = 0.35$ N/W. For a two 1.22 m rotor small rotary wing drone, a parametric study [30] on the cyclic pitch and other variables reports a power loading reaching $\eta_{tot} = 0.143$ N/W. Two recent studies [8, 31] of micro cyclocopters operating at $Re \simeq 11\,000$ and $Re \simeq [20\,000, 40\,000]$ report reaching $\eta_{max} = 0.077$ N/W and $\eta_{tot} = 0.029$ N/W, respectively. Finally, looking at large aerial vehicles designed with multiple flight scenarios in mind, the takeoff weight to maximum power ratios [13] vary from $\eta_{max} = 0.013$ N/W for convertible aircraft to $\eta_{max} = 0.067$ N/W for helicopters. This quick overview indicates that the resulting configuration is difficult to compare with other rotorcraft and disk loading will usually be the determining factor for efficient hover. A more detailed energy analysis could be conducted and take into account predicted aircraft missions with flight patterns and range using parameters from the literature [32], but that remains outside the scope of this preliminary study.

It is noteworthy that the optimized configuration does not have the characteristics reported in a comprehensive experimental study [29] on cycloidal rotor power loading optimization. The study reports optimal power loadings for: high chord/radius ratio; short spans; and, solidity $\sigma \approx 0.4$. This article rather finds very low chord/radius and very low solidity. These discrepancies mostly highlight the different objectives of the two studies and the impact that the weight and material choice have on payload efficiency. As such, a simpler analysis could calculate the aircraft mass m_t by extrapolation. For example, the wing mass extrapolation formula from Roskam [33] fed with the mass and dimensions of a cyclogiro aircraft for which data is available [13] indicate that the current prototype should weight 1.33 kg. This 2.8 times overestimation draws attention to the strong interdependence between the required structural mass and the aerodynamic forces generated by the aircraft. It also confirms that such extrapolation formulas are no longer adequate when the search domain for an energy-efficient solution is not limited to conventional aircraft configurations.



c_{min}	min chord before 100% filled	2.0 cm
c_C	chord to circumf. ratio	0.0288
h_b	blade height	2.41 mm
b_{rod}	rod width x height	0.705 mm x 2.822 mm
R_{fr1i}	inner radius of frame's inner beam	5.80 mm
R_{fr2i}	inner radius of frame's outer beam	1.72 mm
L_{fr}	drone total width	56.0 cm
α_{ma}	max admissible AofA	9.97°
α_{mf}	max AofA	9.97°
σ	rotor solidity	0.0288

Table 6. Optimized geometry.

$\sigma_b _{x=0}$	max midpoint PLA blade stress	28.0 MPa
$w _{x=0}$	max blade center defl.	0.603 mm
EJ_e	composite blade flex. rigidity	0.0311 N/m ²
$\epsilon_b _{x=0}$	max blade midpoint abs. strain	0.992%
ϕ_{bmax}	max torsion delay	0.0217°
τ_{bm}	max torsion-induced stress	24.4 kPa
n_{bt}	blade torsion natural freq.	8196 rad/s
$r_{tbt} n_{bt}$	max allowed torsion blade freq.	735 rad/s
f_{rodmax}	max. tensile forces per rod	13.0 N
T_{rod}	max. torque per rod	1.18 Ncm

Table 7. Optimized structure.

5.2 Exploration domain

The PLA blade of the optimum design operates at yield stress. The aluminum spar's aspect ratio tends to the minimum value of 4% because the optimal design has no need of the spar and it does not contribute to the strength of the blade. Because the blade's inner partially filled PLA portion is infinitesimal compared to its 100% filled skin layers, its Young's modulus from Eq. (27) could in practice reach 3.5 times the calculated value. The blade aspect ratio of the optimal configuration is 1.9. For a fixed-wing aircraft, such a low ratio would yield an increased drag coefficient. However, it is known [23] that the power consumed by a cycloidal rotor with blade aspect ratios varying between 1 and 8 does not vary considerably. The magnitude of the pitch function of the optimal designs consistently reaches the maximum allowed angle of attack for their respective operating Reynolds number. The other constraints presented in Table 3 are amply satisfied. The final variables returned by the optimization given in Table 4 are compared to the allowed ranges of Table 1. This shows that the infill percentages both go to their maximum allowed values. Values of infill percentages larger than 90% were, however, not allowed because they are known to degrade the structural properties. The solution also uses the minimum number of blades, but a single blade design was not allowed, to avoid vibrations.

It is recalled that the rotor angular velocity reported is the one which gives the declared efficiencies, which could be reduced when not flying in hover at maximum payload. It is also far below the maximum allowed frequency for the torsion-induced blade pitch delay. The torsion-induced stress is calculated in the blade using an uncoupled approach, which is deemed a reasonable assumption because the bending and torsional stresses act in different directions and the used limit on the torsion angle is low. A proper coupled stress analysis is, however, recommended before proceeding with an actual design.

The last optimization iterations of the manual multistart approach used the maximum infill percentage values, the minimum blade number, and the minimum spar aspect ratio. A compromise is then obtained between the width of the frame, the span of the blades and the rotor radii. It is, however, clear from the results that the optimum configuration is one with the lowest disk loading and the lowest blade velocity. The final blade span is also small, because larger spans induce more centrifugal forces and consequently require lower angular velocities or stronger blades.

5.3 Numerical aspects

A peculiarity of the optimization is that a small subset of the exploration domain variables generate imaginary solutions to the $\tau_{b_{mc}}$ and $\Omega_{t_{mc}}$ constraint equations. Neither increasing the precision of the C++ code, nor solving the symbolic equations directly, nor computing the whole mathematical derivation from start to finish at each optimization algorithm's function evaluation eliminates the imaginary results. A small penalty is thus used to steer the minimization process away from the few non-real solutions. The compiled C++ code allows multiple thousand function evaluations per second while the symbolic, Python, solution did 2 evaluations per second. Finally, an embedded⁶ optimization approach may be the most effective approach, but was still in early development within the Dakota code when this study was started.

5.4 Possible improvements

Configurations with thicker blade profiles that better resist bending can be evaluated by generating their Reynolds-dependent equations using the previously mentioned XFLR5 based technique. The effect of increasing the battery life and the number of blades and/or rotors is worth studying. Using a cantilever blade with one or two blade ends attached to the pivot rods also deserves attention. A more thorough analysis can consider the weight of a transmission or the increased weight of using four smaller motors instead of one. The unnecessary blade tip pitch rods weight contributions can also be removed. An improved design could allow asymmetric frame arm lengths, thus greatly reducing the frame weight, which currently represent 50% of the complete aircraft weight. The frame weight could also be reduced by using composite materials for its beams or removing the double load assumption of Eq. 69. Alternatively, intermeshing rotors could be considered, but blade vortex and induced velocity interactions may have unpredictable effects. Finally, the number of fully printed layers could be reduced to a single one in order to reduce weight and make the aluminum spar more useful or allow smaller blade chord length.

⁶The embedded approach allows running the GM iteratively within the steps of the GA.



6. Conclusion

This paper presented a novel method to optimize the general parameters of a micro aircraft prior to designing and printing a detailed drone. The effects of geometrical and structural parameters, such as the infill percentages of the printed parts and their sizes, were taken into consideration in an attempt to bring the power to payload ratio to a minimum. A minimization technique with one objective function, 7 constraints, and 10 variables was used to yield an optimal configuration. The resulting configuration was presented in all its detail and the procedure used can be adapted to different cyclogyro designs. The whole procedure was carried out using open source software, mainly the SageMath [24] and Dakota [25] toolboxes. The method can also be modified to perform similar preliminary analyses for other 3D printed aircraft designs that require the optimization of efficiency. Finally, the method easily extends to study supplementary parameters and configurations in order to obtain the best compromise between aircraft size, cost, flight time, flight velocity, efficiency, and payload. The complete code necessary to reproduce the results presented in this paper is available online at <https://github.com/louisgag/cyclogyroOptimization>.

Author Contributions

Louis Gagnon led the project, produced the results, and wrote the article. All authors developed the aircraft concept and mathematical equations together. They also discussed the results, reviewed, and approved the final version of the manuscript.

Conflict of Interest

The authors declared no potential conflicts of interest with respect to the research, authorship and publication of this article.

Funding

Louis Gagnon would like to recognize the funding of the Polimi International Fellowship research grant Index no. 1378 - Ref. No. 15881 made available for the *An aeroelastic study of cycloidal rotors used in various configurations* project which covered the vast majority of the work presented here. Small revisions to the code were made possible through the support of the Alexander von Humboldt Foundation for the *A Novel and Simple Aircraft Requiring Minimal Power to Hover* project.


References


- [1] McNabb, M.L., Development of a Cycloidal Propulsion Computer Model and Comparison with Experiment, Master's thesis, Mississippi State University, 2001.
- [2] Xisto, C.M., Páscoa, J.C., Leger, J.A., Masarati, P., Quaranta, G., Morandini, M., Gagnon, L., Wills, D., Schwaiger, M., Numerical modelling of geometrical effects in the performance of a cycloidal rotor, *6th European Conference on Computational Fluid Dynamics*, Barcelona, Spain.
- [3] Leger, J.A., Páscoa, J.C., Xisto, C.M., Aerodynamic optimization of cyclorotors, *J. of Aircraft Engineering and Aerospace Technology*, 2016.
- [4] Benedict, M., Ramasamy, M., Chopra, I., Leishman, J.G., Experiments on the Optimization of MAV-Scale Cycloidal Rotor Characteristics Towards Improving Their Aerodynamic Performance, *American Helicopter Society International Specialist Meeting on Unmanned Rotorcraft*, Phoenix, Arizona.
- [5] Benedict, M., Ramasamy, M., Chopra, I., Leishman, J.G., Performance of a Cycloidal Rotor Concept for Micro Air Vehicle Applications, *Journal of the American Helicopter Society*, 2010, 55(2), 022002-1-14, doi:10.4050/JAHS.55.022002.
- [6] Benedict, M., Mataboni, M., Chopra, I., Masarati, P., Aeroelastic Analysis of a Micro-Air-Vehicle-Scale Cycloidal Rotor, *AIAA Journal*, 2011, 49(11), 2430-2443, doi:10.2514/1.J050756.
- [7] Lind, A.H., Jarugumilli, T., Benedict, M., Lakshminarayan, V.K., Jones, A.R., Chopra, I., Flow field studies on a micro-air-vehicle-scale cycloidal rotor in forward flight, *Experiments in Fluids*, 2014, 55(12), 1826.
- [8] Runco, C.C., Benedict, M., Development and flight testing of a meso-scale cyclopter, *55th AIAA Aerospace Sciences Meeting*, American Institute of Aeronautics and Astronautics.
- [9] Lee, C.H., Yong Min, S., Lee, J.E., Kim, S.J., Design, analysis, and experimental investigation of a cyclocopter with two rotors, *Journal of Aircraft*, 2016.
- [10] Andrews, G., Shrestha, E., Chopra, I., Design and fabrication of a meso-scale aircraft using a cycloidal rotor propulsion system, *54th AIAA Aerospace Sciences Meeting*, 2016.
- [11] Hu, Y., Zhang, H., Wang, G., Two dimensional and three dimensional numerical simulation of cycloidal propellers in hovering status, *54th AIAA Aerospace Sciences Meeting*, 2016.
- [12] Hu, Y., Du, F., Zhang, H.L., Investigation of unsteady aerodynamics effects in cycloidal rotor using RANS solver, *The Aeronautical Journal*, 2016, 120(1228), 956-970.
- [13] Schwaiger, M., Wills, D., D-dalus vtol - efficiency increase in forward flight, *Aircraft Engineering and Aerospace Technology*, 2016, 88(5), 594-604.
- [14] Xisto, C.M., Leger, J.A., Páscoa, J.C., Gagnon, L., Masarati, P., Angeli, D., Dumas, A., Parametric analysis of a large-scale cycloidal rotor in hovering conditions, *Journal of Aerospace Engineering*, Issue: object: doi:10.1061/as.2017.30.issue-1, revision: rev:1483086060334-90:doi:10.1061/as.2017.30.issue-1, 30(1).
- [15] Gagnon, L., Morandini, M., Quaranta, G., Muscarello, V., Masarati, P., Aerodynamic models for cycloidal rotor analysis, *AEAT*, 2016, 88(2), 215 - 231, doi:10.1108/AEAT-02-2015-0047.
- [16] Gagnon, L., Morandini, M., Quaranta, G., Masarati, P., Xisto, C.M., Páscoa, J.C., Aeroelastic analysis of a cycloidal rotor under various operating conditions, *Journal of Aircraft*, 2018, 55(4), 1675-1688.
- [17] Yun, C.Y., Park, I.K., Lee, H.Y., Jung, J.S., H., I.S., Design of a New Unmanned Aerial Vehicle Cyclocopter, *Journal of the American Helicopter Society*, 2007, 52(1).
- [18] Johnson, W., *Helicopter Theory*, Dover Publications, New York, 1994.
- [19] Jain, P., Abhishek, A., Modeling and simulation of virtual camber in cycloidal rotors, *AIAA Journal*, 2017, 55(4), 1465-1468.
- [20] What is the influence of infill %, layer height and infill pattern on my 3d prints?, <http://my3dmatter.com/influence-infill-layer-height-pattern/>, last Accessed: 02/02/2017.
- [21] Young, W., Budynas, R., Sadegh, A., *Roark's Formulas for Stress and Strain*, McGraw Hill, 2011.
- [22] Gagnon, L., Quaranta, G., Schwaiger, M., Wills, D., Aerodynamic analysis of an unmanned cyclogiro aircraft, *SAE Technical Paper*, SAE International.
- [23] Hu, Y., Fu, X., Zhang, H., Wang, G., Farhat, H., Effects of blade aspect ratio and taper ratio on hovering performance of cycloidal rotor with large blade pitching amplitude, *Chinese Journal of Aeronautics*, 2019, 32(5), 1121-1135.
- [24] Stein, W., et al., *Sage Mathematics Software (Version 9.2)*, The Sage Development Team, 2020, <http://www.sagemath.org>.
- [25] Brian M. Adams and William J. Bohnhoff and Keith R. Dalbey and Mohamed S. Ebeida and John P. Eddy and Michael S. Eldred and Russell W. Hooper and Patricia D. Hough and Kenneth T. Hu and John D. Jakeman and Mohammad Khalil and Kathryn A. Maupin and Jason A. Monschke and Elliott M. Ridgway and Ahmad A. Rushdi and D. Thomas Seidl and J. Adam Stephens and Laura P. Swiler and and Justin G. Winokur, Dakota, a multilevel parallel object-oriented framework for design optimization, parameter estimation, uncertainty quantification, and sensitivity analysis: Version 6.13 user's manual, Tech. rep., Sandia Technical Report SAND2020-12495, 2020.
- [26] Vanderplaats, G.N., CONMIN - a FORTRAN program for constrained function minimization, Tech. rep., NASA Technical Report TM X-62282, 1973.
- [27] Mayo, D.B., Leishman, J.G., Comparison of the hovering efficiency of rotating wing and flapping wing micro air vehicles, *Journal of the American Helicopter Society*, 2010, 55(2), 25001-250015.
- [28] Robertson, C.D., Reichert, T.M., Design and development of the atlas human-powered helicopter, *AIAA Journal*, 2015, 53(1), 20-32.



- [29] Benedict, M., Jarugumilli, T., Chopra, I., Effect of Rotor Geometry and Blade Kinematics on Cycloidal Rotor Hover Performance, *Journal of Aircraft*, 2013, 50(5), 1340–1352, doi:10.2514/1.C031461.
- [30] Shahmiri, F., Twin-rotor hover performance examination using overlap tests, *Aircraft Engineering and Aerospace Technology*, 2017, 89(1), 155–163.
- [31] Shrestha, E., Yeo, D., Benedict, M., Chopra, I., Development of a meso-scale cycloidal-rotor aircraft for micro air vehicle application, *International Journal of Micro Air Vehicles*, 2017, 175682931770204.
- [32] Nangia, R.K., Efficiency parameters for modern commercial aircraft, *The Aeronautical Journal*, 2006, 110(1110), 495–510.
- [33] Roskam, J., *Airplane Design*, no. pt. 5 in *Airplane Design*, DARcorporation, 1999.

ORCID iD

Louis Gagnon  <https://orcid.org/0000-0002-1619-3236>

Marco Morandini  <https://orcid.org/0000-0002-1992-9077>

Stéphane Fournier  <https://orcid.org/>



© 2020 by the authors. Licensee SCU, Ahvaz, Iran. This article is an open access article distributed under the terms and conditions of the Creative Commons Attribution-NonCommercial 4.0 International (CC BY-NC 4.0 license) (<http://creativecommons.org/licenses/by-nc/4.0/>)

How to cite this article: Louis Gagnon, Marco Morandini, Stéphane Fournier. Parametric Optimization of a Cyclogiro Aircraft Design for Efficient Hover with Aeroelastic Considerations, *J. Appl. Comput. Mech.*, 7(3), 2021, 1774-1787. <https://doi.org/10.22055/JACM.2021.35872.2752>

